https://doi.org/10.1038/s41586-019-1114-6

Nanosecond X-ray diffraction of shock-compressed superionic water ice

Marius Millot[1,3]*, Federica Coppari[1,3]*, J. Ryan Rygg[1,2], Antonio Correa Barrios[1], Sebastien Hamel[1], Damian C. Swift[1] & Jon H. Eggert[1]

Since Bridgman's discovery of five solid water (H_2O) ice phases[1] in 1912, studies on the extraordinary polymorphism of H_2O have documented more than seventeen crystalline and several amorphous ice structures[2,3], as well as rich metastability and kinetic effects[4,5]. This unique behaviour is due in part to the geometrical frustration of the weak intermolecular hydrogen bonds and the sizeable quantum motion of the light hydrogen ions (protons). Particularly intriguing is the prediction that H_2O becomes superionic[6–12]—with liquid-like protons diffusing through the solid lattice of oxygen—when subjected to extreme pressures exceeding 100 gigapascals and high temperatures above 2,000 kelvin. Numerical simulations suggest that the characteristic diffusion of the protons through the empty sites of the oxygen solid lattice (1) gives rise to a surprisingly high ionic conductivity above 100 Siemens per centimetre, that is, almost as high as typical metallic (electronic) conductivity, (2) greatly increases the ice melting temperature[7–13] to several thousand kelvin, and (3) favours new ice structures with a close-packed oxygen lattice[13–15]. Because confining such hot and dense H_2O in the laboratory is extremely challenging, experimental data are scarce. Recent optical measurements along the Hugoniot curve (locus of shock states) of water ice VII showed evidence of superionic conduction and thermodynamic signatures for melting[16], but did not confirm the microscopic structure of superionic ice. Here we use laser-driven shockwaves to simultaneously compress and heat liquid water samples to 100–400 gigapascals and 2,000–3,000 kelvin. In situ X-ray diffraction measurements show that under these conditions, water solidifies within a few nanoseconds into nanometre-sized ice grains that exhibit unambiguous evidence for the crystalline oxygen lattice of superionic water ice. The X-ray diffraction data also allow us to document the compressibility of ice at these extreme conditions and a temperature- and pressure-induced phase transformation from a body-centred-cubic ice phase (probably ice X) to a novel face-centred-cubic, superionic ice phase, which we name ice XVIII[2,17].

Our experimental system (Fig. 1) builds on the development of advanced dynamic compression experiments to access high-density, high-temperature states beyond the reach of current static compression methods, and uses the nanosecond, in situ, powder X-ray diffraction (XRD) techniques at the Omega Laser facility[18,19]. Water being quite compressible, single-shock temperature rises very quickly with pressure[16] reaching 6,000 K near 100 GPa (Fig. 1d). Therefore, to create ultrahigh-pressure solid ices in the laboratory, a series of multiple shocks is necessary to realize a quasi-isentropic compression and to minimize the temperature increase[20,21].

Six high-power laser beams are fired in a temporally tailored sequence about 15 ns long to launch a series of compression shockwaves into a thin water layer encapsulated between a diamond ablator and a diamond window (Fig. 1a). The multiple shockwaves reverberate between the two stiff diamonds to achieve a homogeneous quasi-isentropic compression of the water layer[20,21] (Fig. 2a).

Adjusting the energy and timing of the drive-laser beams on each laser shot, water is compressed to ten different pressure–temperature states in the ranges 100–420 GPa and about 2,000–3,000 K. Ultrafast Doppler velocimetry monitors the compression history on each shot: a two-channel, line-imaging Velocity Interferometer System for Any Reflector (VISAR) records the arrival and exit times of the leading shock in the water sample layer, and encodes the time history of the velocity of the diamond window free surface, $u_{FS}(t)$, which is progressively accelerated by the arrival of the successive compression shockwaves (Figs. 1c, 2a, and Supplementary Fig. 1).

Radiation-hydrodynamic simulations are performed for each laser experiment (Fig. 2). An iterative optimization of the drive-laser intensity input allows us to reproduce the measured timing and amplitude of the successive shocks determined by analysis of the velocimetry data. Once a good match between the measured and computed free-surface velocity history $u_{FS}(t)$ is obtained (Supplementary Fig. 3a), we interrogate the simulations to determine the pressure–temperature compression path experienced by the H_2O sample and the pressure–temperature conditions during the XRD snapshot using the timing of the X-ray pulse (Supplementary Fig. 3). The simulations indicate that the XRD data were collected along two quasi-isentropic paths near 2,000 K and 3,000 K, depending on the strength of the first shockwave reaching the water layer and on the timing of the main compression pulse.

The atomic structure of dynamically compressed H_2O is characterized in situ using angular dispersive XRD recorded on multiple image plate detector panels (Fig. 1b). Focusing 16 laser beams on an iron (Fe) foil generates an intense X-ray pulse at 6.7 keV resulting from helium (He)-like atomic transitions. About 2×10^{12} X-ray photons are collimated by the 500-μm-diameter tantalum (Ta) aperture placed immediately behind the target package (Fig. 1a). Diffraction off the walls of the Ta pinhole imprints a zero-pressure XRD reference pattern, superimposed on the XRD signal coming from the H_2O sample on the image plates. On each shot, the timing of the 1-ns-long X-ray pulse is adjusted to capture the structure of water near peak compression, typically 10–15 ns after the first shockwave arrival in H_2O (Figs. 1 and 2a).

Figure 3 shows representative XRD images from four different experiments, projected into the Bragg angle (2θ)–azimuthal angle (φ) space. One diffraction line, which we attribute to H_2O ice, is found in the XRD patterns recorded for all ten shots and demonstrates the solidification of a macroscopic fraction of the water sample into a crystalline solid (see Supplementary Information sections S4 and S5 for a detailed description of all the XRD data).

Interrogating the hydrodynamic simulations reveals that the growth time delay (Δt) between the instant H_2O is brought into the stability field of ice and the time of the XRD snapshot (see Fig. 2b and values in Supplementary Table 2) ranges between 2 ns and 5 ns in our experiments. This puts an upper bound on the nucleation of ice near 2 ns. This is faster than previous studies on water ice at much lower pressure[20,22,23] and can be interpreted as a signature for the large over-pressurization

---

[1]Lawrence Livermore National Laboratory, Livermore, CA, USA. [2]Laboratory for Laser Energetics and Department of Mechanical Engineering, University of Rochester, Rochester, NY, USA. [3]These authors contributed equally: Marius Millot, Federica Coppari. *e-mail: millot1@llnl.gov; coppari1@llnl.gov

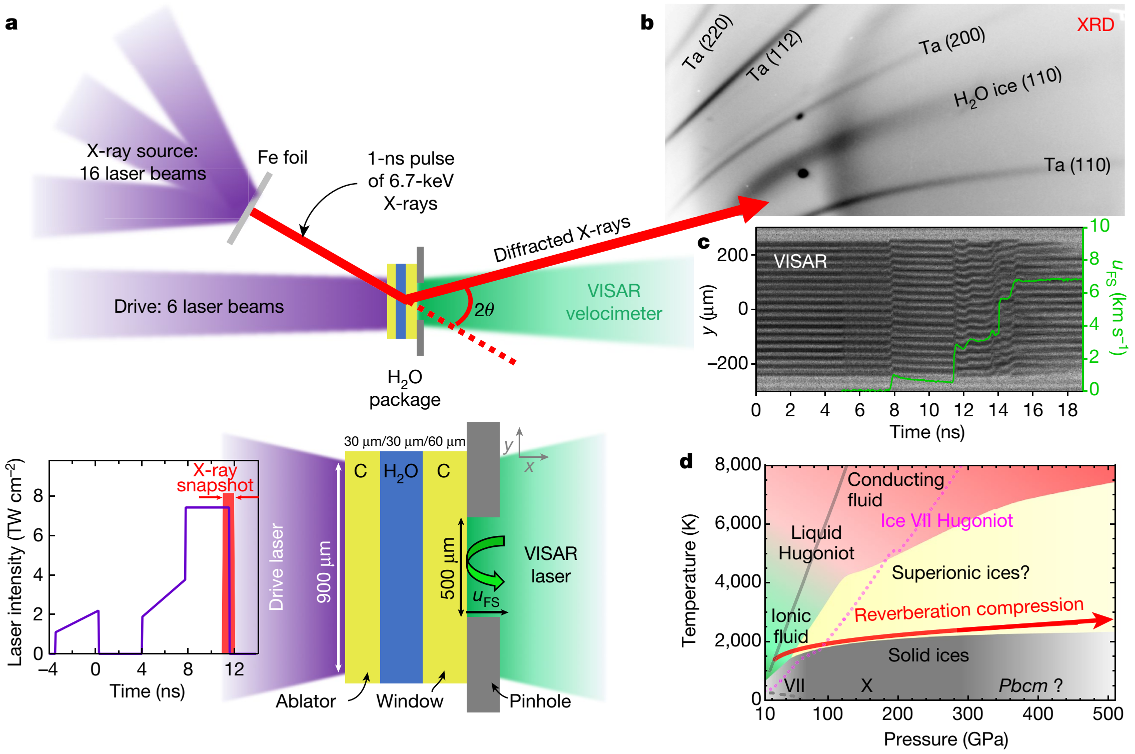

Fig. 1 | Experimental concept (not to scale). a, A series of laser pulses generates a multi-shock compression sequence of the initially liquid water layer. Additional laser beams generate a X-ray flash off an iron foil. **b**, Image plates record the X-ray diffraction snapshot documenting the solidification of the initially liquid water during the dynamic loading. Ambient-pressure diffraction lines from the Ta pinhole are used to calibrate the diffraction geometry (data from shot 73144). **c**, A line-imaging velocimeter (VISAR) monitors the diamond window free-surface velocity history $u_{FS}(t)$ from which the pressure–temperature compression path is reconstructed. **d**, The reverberation compression scheme enables the phase diagram of H_2O at extreme pressure–temperature conditions to be explored.

(far into the solid stability field): the large free-energy difference favouring ice over liquid water drives the rapid solidification.

Figures 1b and 3a also reveal that the diffraction peaks from H_2O are broader than the zero-pressure Ta reference lines, whose width is dominated by the experimental angular resolution in 2θ and geometrical effects (contributing to about 0.8°). Because we observe only the most intense XRD peak for water ice, we cannot formally disentangle the respective strain and grain-size contributions to the peak broadening. However, assuming that grain-size effects solely determine the angular broadening and using the Scherrer equation with the full-width at half-maximum (FWHM) of the H_2O line provides a lower bound for the typical grain (crystallite) size D of about 4–7 nm (see Supplementary Information sections S4 and S6). This is similar to recent observations in laser-driven shock crystallization of glassy SiO_2 (ref. [24]) and is also consistent with billion-atom molecular dynamics simulations of strongly undercooled iron melt, indicating freezing by homogeneous nucleation within about 200 ps followed by competitive coalescence growth[25] of approximately 5–10-nm-sized grains within 1–2 ns.

The d-spacing of the observed H_2O XRD line and its decrease upon pressure increase from 101 GPa to 249 GPa along the quasi-isentrope near 2,000 K are consistent with the most intense (110) reflection of the body-centred-cubic (b.c.c.) oxygen lattice of ice X (Fig. 3b, blue circles). Indeed, the experimental d-spacing and density–pressure dependences agree with both experimental-based[26] and density functional theory (DFT)-based equation-of-state models[27] (black dashed line and blue dotted line in Fig. 3b and c, respectively).

At higher pressure along the same quasi-isentrope near 2,000 K, the data reveal a jump in the d-spacing of about 0.05 Å between 249 GPa and 278 GPa followed by a compression-driven decrease up to 420 GPa, pointing to a structural phase transformation (red circles in Fig. 3b). The observed XRD line above 278 GPa most probably corresponds to the (111) reflection off a close-packed ice structure with a face-centred-cubic (f.c.c.) lattice of oxygen atoms (see Supplementary Table 2). Attributing the observed XRD line to other potentially expected structures would result in very large, unrealistic density jumps above 249 GPa (see Supplementary Information section S5). Interpreting the new phase as f.c.c. does not produce a substantial discontinuity in the pressure–density relation for dense H_2O at the b.c.c.–f.c.c. transition (within the uncertainty of our measurement), consistent with the expected small volume jump for this phase change[15], indicative of the novel f.c.c. structure having a volume compressibility similar to that of ice X.

The two XRD patterns recorded near 3,000 K (red squares in Fig. 3b, c) are also consistent with the same f.c.c. structure. Showing the results of the XRD experiments on the phase diagram of dense H_2O (Fig. 4) indicates that both pressure (between 249 GPa and 278 GPa) and temperature (between about 2,000 K and about 3,000 K) can induce the transformation of b.c.c. H_2O ice into the novel f.c.c. phase that we propose to name ice XVIII (see Supplementary Table 1 in Supplementary Information section S7).

Figure 4 also shows that the pressure and temperature of (at least) one of our XRD measurements—near 160 GPa and 3,200 K—overlap with the conditions where superionic conduction has recently been experimentally observed[16]. The new ice (ice XVIII) is therefore very likely to be superionic and the XRD data provide direct experimental evidence for a crystalline sublattice formed by the oxygen atoms in superionic water ice.

The present XRD dataset also confirms two additional predictions from computer simulations for superionic water ice. First, it confirms the prediction[13–15] that the extra entropy associated with the mobile protons favours novel close-packed structures—such as f.c.c. ice XVIII—above about 100 GPa. In contrast, a f.c.c. lattice is not expected in insulating ice in this pressure range because body-centred-cubic ice X should be stable to at least 300 GPa, before transforming to space group *Pbcm*[28–31]. Second, it confirms the prediction[8–11,13,15] that superionic

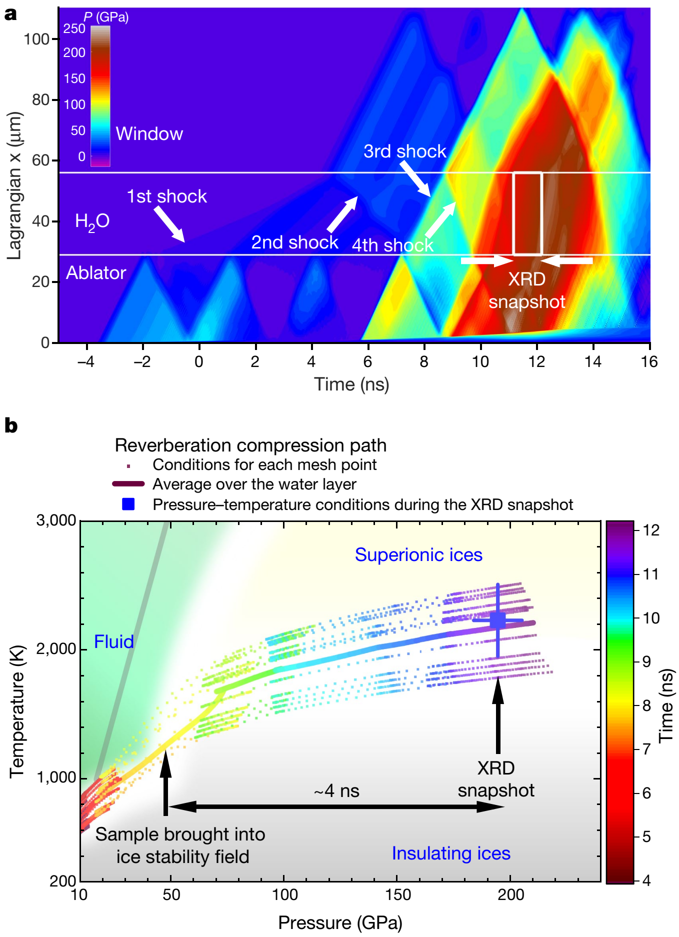

Fig. 2 | Determination of the reverberation compression path using one-dimensional Lagrangian radiation hydrodynamic simulations. **a**, Example space-time contour map of the longitudinal stress for shot 75758: a series of shockwaves compresses the initially liquid water layer before the XRD snapshot at $t \approx 11$ ns (white rectangle). **b**, Calculated pressure–temperature compression paths experienced by each simulation mesh element (dotted lines), and average for the water layer (solid line), with time as a colour scale. The XRD snapshot was taken just a few nanoseconds after H_2O has been dynamically compressed into the predicted stability field of superionic ice[11,15] (black arrows). The final estimate of pressure and temperature during the XRD snapshot is indicated by the blue square, with error bars representing the standard deviation of the distribution of states during the X-ray exposure.

ice can sustain higher temperatures before melting at high pressures, leading to a rapid increase of the melting line above 1,000 K and 50 GPa. Our XRD data up to 320 GPa and 3,800 K provide unambiguous lower bounds for the melting line of water ice at high pressure (Fig. 4), in agreement with previous static compression experiments at lower pressure and the observation of two thermodynamic anomalies near 4,800 K and 190 GPa along the Hugoniot of pre-compressed ice VII[16].

Figure 4 further indicates that the pressure–temperature conditions for the b.c.c. phase data lie in the vicinity of the predicted boundary between solid insulating and superionic ices[15] (grey dashed line). Since temperature-driven phase transitions are more likely to favour transformations from a close-packed to an open, higher-entropy structure upon temperature increase (for example, f.c.c. to b.c.c.), rather than b.c.c. to f.c.c. (as we observe in our experiments), the data collected in the b.c.c. phase are better interpreted as insulating solid ice. If, from a thermodynamic point of view, a temperature-induced superionic b.c.c.-to-superionic f.c.c. transition seems unlikely, the extra entropy of the diffusing protons could, on the other hand, favour a temperature-driven transformation of insulating b.c.c. to superionic f.c.c. near 200 GPa.

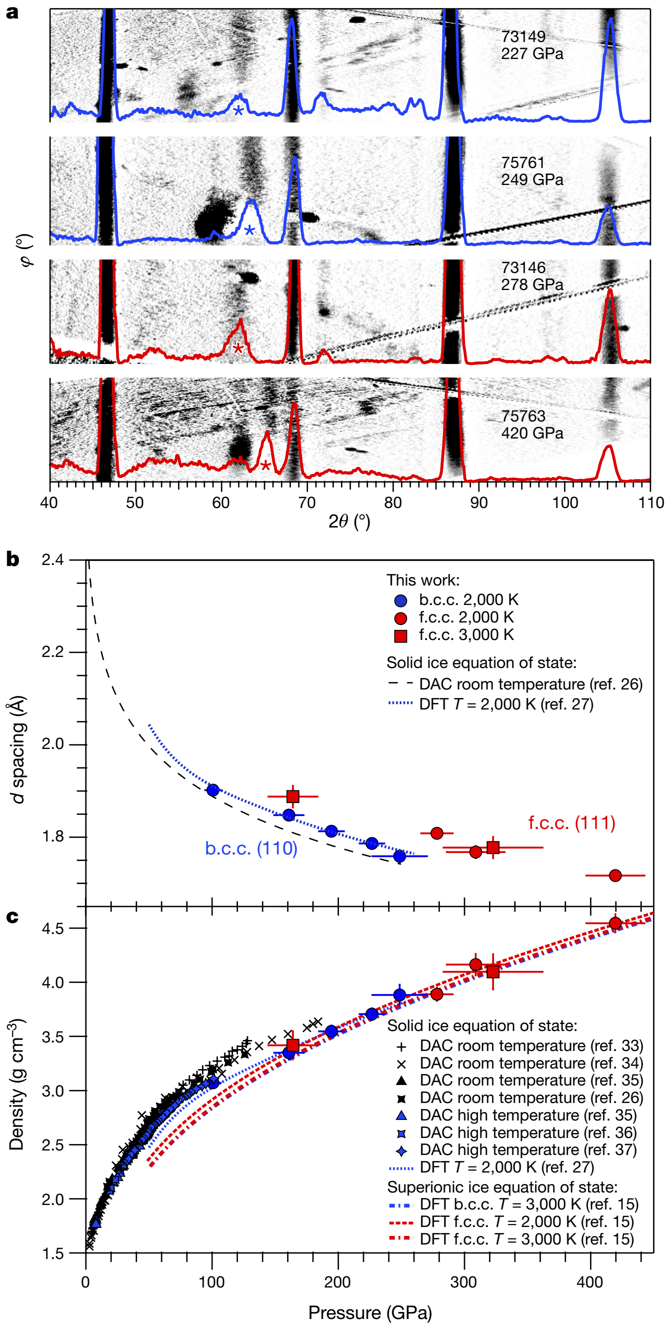

Fig. 3 | X-ray diffraction data and results. **a**, Representative data projected onto 2θ–φ space and the overlaid one-dimensional integration showing the evolution of the diffraction line for water (asterisks) with pressure along the quasi-isentrope near 2,000 K (blue for b.c.c. and red for f.c.c.). See Supplementary Information section S4 and Supplementary Figs 5 and 6 for the complete peak assignment. **b**, Pressure dependence of the measured *d*-spacing. Literature data are taken from refs [26,27]. A discontinuity is observed at 278 GPa along the quasi-isentrope near 2,000 K (blue and red circles for b.c.c. and f.c.c. respectively). Near 3,000 K the *d*-spacing is consistent with the high-pressure f.c.c. structure (red squares). Typical uncertainties are less than about 0.01 Å, smaller than the size of the markers. DAC, diamond anvil cell. **c**, Pressure–density experimental data compared with previous data and computed isotherms. Data are taken from refs [15,26,27,33–37]. Error bars represent 1σ uncertainty for each experiment; see Supplementary Information for a detailed discussion.

The XRD data collected near 100 GPa and 2,000 K—that is, along the ice VII Hugoniot, very close to the conditions where superionic conduction was experimentally documented[16]—might indicate that a b.c.c. superionic ice exists below 160 GPa, as suggested by simulations[12–15].

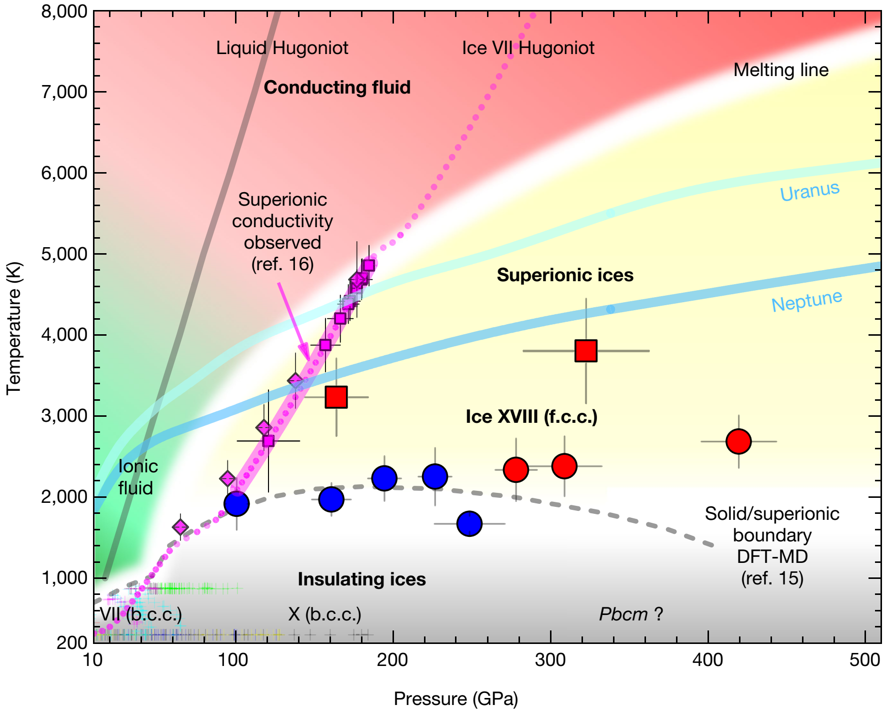

Fig. 4 | Phase diagram of H_2O. Pressure–temperature conditions of the XRD measurements in the b.c.c. phase (blue circles) and in the novel f.c.c. superionic ice, ice XVIII (red circles and squares, near 2,000 K and 3,000 K, respectively). Conductivity measurements with precompressed shocks[16] (magenta squares) and reverberating shocks[21] (magenta diamonds) have demonstrated superionic conduction between 100 GPa and 190 GPa along the ice VII Hugoniot. Coloured crosses indicate pressure–temperature conditions for static compression XRD experiments (see details in Supplementary Fig. 18). Planetary interior conditions for Neptune and Uranus from ref. [32] are also shown. The predicted boundary between solid and f.c.c. superionic ice[15] is represented by the dashed grey line. Error bars represent 1σ uncertainty for each experiment; see Supplementary Information for a detailed discussion.

However, more data at higher temperature in this pressure range are needed to remove any ambiguities.

This study brings the last missing piece to the puzzle regarding the existence of superionic water ice, 30 years after the original prediction[6], and directly documents the presence of a crystalline lattice in superionic ice at the extreme pressures and temperatures relevant for the deep interior of Neptune, Uranus and icy giant exoplanets. Given that H_2O is believed to constitute about 65% by mass of Uranus and Neptune, comparing the interior isentropes from ref. [32] with the experimentally constrained melting line on Fig. 4 confirms the prediction[10,11,13] that superionic ice could indeed be stable at depths greater than about 8,000 km (roughly one-third of the radius of Uranus and Neptune) and contribute to forming a thick solid icy mantle in these planets.

The observation of a crystalline lattice of oxygens indicates that superionic water ice should indeed behave similarly to a solid, with a viscosity several orders of magnitude larger than typical fluid values. This finding is supported by computing the elastic constants with DFT-based molecular dynamics (DFT-MD) up to 450 GPa at 4,000 K (see Supplementary Information section S8). The calculation shows that the shear modulus of superionic ice is slightly lower than that of insulating ice X but evolves similarly with increasing pressure (see Supplementary Fig. 24). Therefore, the characteristics of superionic ice flows within Neptune and Uranus are likely to be more similar to those of slow convection within the solid Earth mantle than to those of the rapid swirls of fluid iron in the Earth's outer core.

Online content

Any methods, additional references, Nature Research reporting summaries, source data, statements of data availability and associated accession codes are available at https://doi.org/10.1038/s41586-019-1114-6.

Received: 27 October 2017; Accepted: 8 February 2019;
Published online 8 May 2019.

1. Bridgman, P. W. Water, in the liquid and five solid forms, under pressure. *Proc. Am. Acad. Arts Sci.* **47**, 441–558 (1912).
2. Bartels-Rausch, T. et al. Ice structures, patterns, and processes: a view across the icefields. *Rev. Mod. Phys.* **84**, 885–944 (2012).
3. Malenkov, G. Liquid water and ices: understanding the structure and physical properties. *J. Phys. Condens. Matter* **21**, 283101 (2009).
4. Pallares, G. et al. Anomalies in bulk supercooled water at negative pressure. *Proc. Natl Acad. Sci. USA* **111**, 7936–7941 (2014).
5. Mishima, O. & Stanley, H. E. The relationship between liquid, supercooled and glassy water. *Nature* **396**, 329–335 (1998).
6. Demontis, P., LeSar, R. & Klein, M. L. New high-pressure phases of ice. *Phys. Rev. Lett.* **60**, 2284–2287 (1988).
7. Cavazzoni, C. et al. Superionic and metallic states of water and ammonia at giant planet conditions. *Science* **283**, 44–46 (1999).
8. Mattsson, T. R. & Desjarlais, M. P. Phase diagram and electrical conductivity of high energy-density water from density functional theory. *Phys. Rev. Lett.* **97**, 017801 (2006).
9. Schwegler, E., Sharma, M., Gygi, F. & Galli, G. Melting of ice under pressure. *Proc. Natl Acad. Sci. USA* **105**, 14779–14783 (2008).
10. French, M., Mattsson, T., Nettelmann, N. & Redmer, R. Equation of state and phase diagram of water at ultrahigh pressures as in planetary interiors. *Phys. Rev. B* **79**, 054107 (2009).
11. Redmer, R., Mattsson, T. R., Nettelmann, N. & French, M. The phase diagram of water and the magnetic fields of Uranus and Neptune. *Icarus* **211**, 798–803 (2011).
12. Hernandez, J.-A. & Caracas, R. Superionic-superionic phase transitions in body-centered cubic H_2O ice. *Phys. Rev. Lett.* **117**, 135503 (2016).
13. Wilson, H. F., Wong, M. L. & Militzer, B. Superionic to superionic phase change in water: consequences for the interiors of Uranus and Neptune. *Phys. Rev. Lett.* **110**, 151102 (2013).
14. Sun, J., Clark, B. K., Torquato, S. & Car, R. The phase diagram of high-pressure superionic ice. *Nat. Commun.* **6**, 8156 (2015).
15. French, M., Desjarlais, M. P. & Redmer, R. *Ab initio* calculation of thermodynamic potentials and entropies for superionic water. *Phys. Rev. E* **93**, 022140 (2016).
16. Millot, M. et al. Experimental evidence for superionic water ice using shock compression. *Nat. Phys.* **14**, 297–302 (2018).
17. del Rosso, L., Celli, M. & Ulivi, L. A new porous water ice stable at atmospheric pressure obtained by emptying a hydrogen filled ice. *Nat. Commun.* **7**, 1–19 (2016).
18. Rygg, J. R. et al. Powder diffraction from solids in the terapascal regime. *Rev. Sci. Instrum.* **83**, 113904 (2012).
19. Coppari, F. et al. Experimental evidence for a phase transition in magnesium oxide at exoplanet pressures. *Nat. Geosci.* **6**, 926–929 (2013).
20. Dolan, D. H. & Gupta, Y. M. Nanosecond freezing of water under multiple shock wave compression: optical transmission and imaging measurements. *J. Chem. Phys.* **121**, 9050–9057 (2004).

21. Chau, R., Mitchell, A. C., Minich, R. W. & Nellis, W. J. Electrical conductivity of water compressed dynamically to pressures of 70–180 GPa (0.7–1.8 Mbar). *J. Chem. Phys*. **114**, 1361–1365 (2001).
22. Dolan, D. H., Knudson, M. D., Hall, C. A. & Deeney, C. A metastable limit for compressed liquid water. *Nat. Phys*. **3**, 339–342 (2007).
23. Gleason, A. E. et al. Compression freezing kinetics of water to ice VII. *Phys. Rev. Lett*. **119**, 025701 (2017).
24. Gleason, A. E. et al. Ultrafast visualization of crystallization and grain growth in shock-compressed SiO_2. *Nat. Commun*. **6**, 8191 (2015).
25. Shibuta, Y. et al. Heterogeneity in homogeneous nucleation from billion-atom molecular dynamics simulation of solidification of pure metal. *Nat. Commun*. **8**, 10 (2017).
26. Sugimura, E. et al. Compression of H_2O ice to 126 GPa and implications for hydrogen-bond symmetrization: synchrotron X-ray diffraction measurements and density-functional calculations. *Phys. Rev. B* **77**, 214103 (2008).
27. French, M. & Redmer, R. Construction of a thermodynamic potential for the water ices VII and X. *Phys. Rev. B* **91**, 014308 (2015).
28. Benoit, M., Bernasconi, M., Focher, P. & Parrinello, M. New high-pressure phase of ice. *Phys. Rev. Lett*. **76**, 2934–2936 (1996).
29. Caracas, R. Dynamical instabilities of ice X. *Phys. Rev. Lett*. **101**, 085502 (2008).
30. Militzer, B. & Wilson, H. F. New phases of water ice predicted at megabar pressures. *Phys. Rev. Lett*. **105**, 195701 (2010).
31. Hermann, A., Ashcroft, N. W. & Hoffmann, R. High pressure ices. *Proc. Natl Acad. Sci. USA* **109**, 745–750 (2012).
32. Nettelmann, N., Helled, R., Fortney, J. J. & Redmer, R. New indication for a dichotomy in the interior structure of Uranus and Neptune from the application of modified shape and rotation data. *Planet. Space Sci*. **77**, 143–151 (2013).
33. Hemley, R. J. et al. Static compression of H2O-ice to 128 GPa (1.28 Mbar). *Nature* **330**, 737–740 (1987).
34. Loubeyre, P., LeToullec, R., Wolanin, E., Hanfland, M. & Hausermann, D. Modulated phases and proton centring in ice observed by X-ray diffraction up to 170 GPa. *Nature* **397**, 503–506 (1999).
35. Frank, M. R. M., Fei, Y. & Hu, J. Constraining the equation of state of fluid H_2O to 80 GPa using the melting curve, bulk modulus, and thermal expansivity of ice VII. *Geochim. Cosmochim. Acta* **68**, 2781–2790 (2004).
36. Sugimura, E. et al. Simultaneous high-pressure and high-temperature volume measurements of ice VII and its thermal equation of state. *Phys. Rev. B* **82**, 134103 (2010).
37. Sugimura, E. et al. Experimental evidence of superionic conduction in H_2O ice. *J. Chem. Phys*. **137**, 194505 (2012).

Acknowledgements We acknowledge C. Davis, J. Emig, E. Folsom, R. Posadas Soriano, S. Uhlich, T. Uphaus and W. Unites for target preparation, the Omega Laser Facility management, staff and support crew for shot and diagnostic support and G. W. Collins, F. Datchi, R. Jeanloz and P. F. McMillan for discussions. This work was prepared by LLNL under contract DE-AC52-07NA27344. Omega shots were allocated through the LLE Laboratory Basic Science programme. Partial support was provided by LLNL LDRD programmes 12-SI-007, 14-SI-003 and 19-ERD-031 and the US Department of Energy through the joint FES/NNSA HEDLP programme.

Reviewer information *Nature* thanks Stephane Mazevet and the other anonymous reviewer(s) for their contribution to the peer review of this work.

Author contributions M.M. and F.C. contributed equally to this work, designed and fielded the laser shots, analysed the data and wrote the manuscript. M.M. initiated the project and performed hydrodynamic simulations (with input from D.C.S.). A.C.B. prepared the water targets. J.R.R. was the principal investigator of the Omega laser experimental campaign. S.H. performed molecular dynamics numerical simulations. J.H.E., J.R.R. and F.C. contributed to the development of the diffraction data analysis software. All authors discussed the data analysis and interpretation and commented on the manuscript.

Competing interests The authors declare no competing interests.

Additional information

Supplementary information is available for this paper at https://doi.org/10.1038/s41586-019-1114-6.
Reprints and permissions information is available at http://www.nature.com/reprints.
Correspondence and requests for materials should be addressed to M.M. or F.C.

Publisher's note: Springer Nature remains neutral with regard to jurisdictional claims in published maps and institutional affiliations.

© This is a U.S. government work and not under copyright protection in the U.S.; foreign copyright protection may apply 2019